Results in Physics 52 (2023) 106845

Contents lists available at ScienceDirect

Results in Physics

journal homepage: www.elsevier.com/locate/rinp

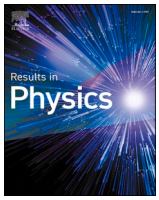

Structure and diffuseness model of solid-liquid interface for binary alloys

Yaw Delali Bensah *

Department of Materials Science and Engineering, School of Engineering Sciences, University of Ghana, Legon-Accra GA490, Ghana

ARTICLE INFO

Keywords:
Maximum entropy production rate (MEPR)
Planar morphology
Cellular morphology
Facet/non-facet morphological transition
Solid–liquid interface

ABSTRACT

Using the morphological instability at the solid–liquid interface as a basis by the maximum entropy production rate principle (MEPR), a model is presented on the morphological structure and diffuseness of the interface during directional solidification of binary alloys. It is shown that, the independent diffuseness theory of Cahn and the Jackson roughness criterion can be unified at a limiting condition under this new MEPR solidification model. The model under the principle of MEPR is applied to describe the evolution of atomistically smooth and rough interfaces through the evaluation of the size of the solid–liquid interface and the of number atomic layers. The model is tested with data for binary alloys of aluminium, lead, and tin at varying solute concentrations. The results showed strong agreement with available data from experimental measurements.

Introduction

The concept of interface diffuseness

The solid–liquid interface (SLI) or simply interface is described as the region that is established between the fully solid and fully liquid boundaries for the solidification of a binary alloy. The interface contains hidden information about microstructural features which can evolve when changes in solidification velocity is accompanied by variations in topography leading to the appearance of a non-faceted cellular or faceted cellular morphology from a planar front interface. However, the concept of SLI [1] and the corresponding thickness (size) is not usually factored into the study of microstructural evolution of liquid–solid transformation except in the pioneering work of Cahn [2,3], the phase field model [4] and the principle of maximum entropy production rate (MEPR) discussions on solidification [1,5,6,7,8,9]. The seminal works of Frank [9], and Burton, Cabrera, Frank [10] (commonly referred to as the BCF theory) described crystal/solid–liquid interfaces as belonging to singular, vicinal, and non-singular class of surfaces. The work of Cahn [2,3] classified solid–liquid interfaces as either atomistically smooth (sharp interface) or atomistically rough (diffuse interface) and showed that a transition between smooth and rough could be enabled by an increased driving force for transformation (i.e. an increased solidification velocity) [2,3]. Cahn introduced a diffuseness parameter, g_m (dimensionless), and predicted that when $g_m = 1$, atomistically smooth interface occurs which display macroscopically faceting morphology during growth. This morphology has an appearance of flat sided faces that rely on step-like growth defects for propagation, such as provided by dislocations and ledges. On the other hand, when $g_m < 1$, atomistically rough interface occurs which display macroscopically non-faceted morphology. Cahn further showed that, the interface diffuseness parameter is a function of the solidification velocity which is the driving force for transformation for the case of directional solidification.

On previous analysis of interface diffuseness

In an earlier study on the analysis on how the size of the SLI fluctuates with the solidification growth velocity, it was shown that the a diffuseness parameter, g_m (dimensionless), which is also named, Cahn diffuseness parameter [11] is given by [2,3],

$$g_m = 2\pi^4 \eta_G^3 \exp\left(\frac{-\pi^2 \eta_G}{2}\right) \tag{1}$$

where the η_G (dimensionless) as described by Cahn is the size of the SLI, ζ (m) in terms of the number of crystallographic lattice planes (or the number of atomic layers). The parameter η_G has also been previously named as the Cahn driving force diffuseness [11] which is given as [2,3],

$$\eta_G = \frac{\zeta}{d} \tag{2}$$

where d (m) is the interplanar spacing of the crystallographic growth plane preferably along the closed packed plane considered as a reasonable length scale for normalization of the size of the SLI. As was discussed by Cahn in the treatment of interface diffuseness, the forma-

* Corresponding author.
E-mail address: ydbensah@ug.edu.gh.

https://doi.org/10.1016/j.rinp.2023.106845
Received 24 June 2023; Received in revised form 1 August 2023; Accepted 7 August 2023
Available online 18 August 2023

List of symbols

General symbols

A_{SLI} (m^2) area of the solid-liquid interface (SLI)
A_W ($Kgmol^{-1}$) atomic weight
C_O ($molm^{-3}$) initial solute concentration in the binary alloy material
d (m) interplanar spacing
g_m (dimensionless) Cahn diffuseness parameter
D_L (m^2s^{-1}) diffusion coefficient of solute in a solvent
G_S (K/m) temperature gradient in the solid
G_L (K/m) temperature gradient in the liquid
G_{SLI} (Km^{-1}) linear temperature gradient across the SLI
Δh_{sl} (J/m^{-3}) heat of fusion
Δh_m (J/mol) heat of fusion
k (no units) partition coefficient
M_d (dimensionless) constant
M_{dc} (dimensionless) constant at morphological instability
B_d (dimensionless) constant
m_L (Km^3 $mole^{-1}$) slope of the liquidus line at the solid–liquid boundary for a binary alloy
$\dot{s}_{gen}$ ($J\ m^{-3}K^{-1}s^{-1}$) total entropy generation rate density at the SLI
$\dot{s}_{LG}$($J\ m^{-3}K^{-1}$) entropy generation rate density by force-flux due to the solute gradient in the liquid
$\dot{s}_E$($J\ m^{-3}K^{-1}$) entropy generation rate density due to exchange of matter at the SLI
$\dot{s}_{in}$ ($J\ K^{-1}s^{-1}$) rate of entropy entering a control volume
$\dot{s}_{out}$ ($J\ K^{-1}s^{-1}$) rate of entropy leaving a control volume
$\dot{s}_{gen}$ ($J\ K^{-1}s^{-1}$) irreversible entropy generation rate in the SLI
s_{LG} ($J\ m^{-3}\ K^{-1}$) entropy generation density due to solute gradient in the liquid
s_{SG} ($J\ m^{-3}\ K^{-1}$) entropy generation density due to solute gradient in the solid
T_m (K) melting temperature
T_l (K) liquidus temperature
T_s (K) solidus temperatures
T_{li} (K) liquidus temperature at the boundary of the SLI
T_{si} (K) solidus temperatures at the boundary of the SLI
ΔT_O (K) solidification temperature range
ΔT_{SLI} (K) temperature difference across the SLI
R_g ($J/mole\ K^{-1}$) universal gas constant
V (ms^{-1}) solidification velocity
V_C (ms^{-1}) solidification velocity at instability
$\frac{dS_{cv}}{dt}$ ($J\ K^{-1}s^{-1}$) total steady state entropy rate change in a control volume

Greek symbols

$\dot{\varphi}_{max}$($Jm^{-3}K^{-1}s^{-1}$) maximum entropy generation rate density
$\Delta\rho_k$ ($kg\ m^{-3}$) overall density shrinkage
$\Delta\rho$ ($kg\ m^{-3}$) density change from liquid to solid
ρ_s ($kg\ m^{-3}$) density of the fully solid state
ρ_l ($kg\ m^{-3}$) density of the fully liquid sate
ζ (m) thickness of the solid–liquid interface (SLI)
η_G (dimensionless) Cahn driving force diffuseness
η_α (dimensionless) Jackson thermal diffuseness
η_T (dimensionless) total diffuseness
α_J (dimensionless) Jackson roughness factor
ω_D ($J\ m^{-3}$) energy of defects
Ω_{SLI} (m^3) volume of the SLI

Acronyms

MEPR maximum entropy rate density
SLI solid–liquid interface
LG solute gradient in the liquid
SG solute gradient in the solid
Max maximum

tion of a faceted or non-faceted morphology by the Cahn theory can be predicted based on the Cahn diffuseness parameter however, a more exact criterion can be established by considering the Cahn driving force diffuseness (η_G). Thus, the Cahn diffuseness concept (equation (1) can be analyzed to understand how g_m changes with η_G by taking a derivative of equation (1) with respect to η_G, which gives [11],

$$dg_m = 6\pi^4\eta_G^2\exp\left(-\frac{\pi^2\eta_G}{2}\right)d\eta_G - \pi^6\eta_G^3\exp\left(-\frac{\pi^2\eta_G}{2}\right)d\eta_G \tag{3a}$$

From equation (3a) it is expected that dg_m can change from g_m to a maximum of one for the entire range for atomistically smooth interface and atomistically rough interface. The values of g_m can be any minimum but negative value are excluded since it may not have any practical meaning and its importance was not mentioned or highlighted by Cahn. Also, the changes for η_G on the right hand side (RHS) of equation (3a) can be summed up for the contributions of the formation of atomistically smooth interface (leading to cellular faceted morphology) and atomistically rough interface (leading to non-faceted cellular morphology). In this respect, η_G is expected to be very small as zero and can grow up to one ($0 \rightarrow 1$) for the formation of atomistiscally smooth interface. For the formation of atomistically rough interface, η_G is expected to grow from zero to infinity ($0 \rightarrow \infty$) [11]. Therefore, integrating equation (3a) by the limits set for dg_m and $d\eta_G$ gives [11],

$$\int_{g_m}^{1} dg_m = \left[6\pi^4\int_0^1\eta_G^2\exp\left(\frac{-\pi^2\eta_G}{2}\right)d\eta_G - \pi^6\int_0^1\eta_G^3\exp\left(\frac{-\pi^2\eta_G}{2}\right)d\eta_G\right] + \left[6\pi^4\int_0^\infty\eta_G^2\exp\left(\frac{-\pi^2\eta_G}{2}\right)d\eta_G - \pi^6\int_0^\infty\eta_G^3\exp\left(\frac{-\pi^2\eta_G}{2}\right)d\eta_G\right]$$

$$|1-g_m| = 6\pi^4\frac{2!}{(\pi^2/2)^3}\left[1-\sum_{i=0}^{\eta_G=2}\frac{\left(\frac{\pi^2}{2}\right)^0}{0!}+\frac{\left(\frac{\pi^2}{2}\right)^1}{1!}+\frac{\left(\frac{\pi^2}{2}\right)^2}{2!}\right] - \pi^6\frac{3!}{(\pi^2/2)^4}\left[1-\sum_{i=0}^{\eta_G=3}\frac{\left(\frac{\pi^2}{2}\right)^0}{0!}+\frac{\left(\frac{\pi^2}{2}\right)^1}{1!}+\frac{\left(\frac{\pi^2}{2}\right)^2}{2!}+\frac{\left(\frac{\pi^2}{2}\right)^3}{3!}\right] + 6\pi^4\frac{2!}{(\pi^2/2)^3} - \pi^6\frac{3!}{(\pi^2/2)^4}$$

Simplifying the above expression gives,

$$|g_m| = 0.399 \tag{3b}$$

Putting back equation (3b) into equation (1) or (from a plot of g_m against η_G as per equation-1), give two solutions to the Cahn driving force diffuseness (η_G), that is, η_G equal to 0.17 and 1.5, respectively. From the two solutions of η_G, the latter is preferred as it is the maximum value and sets the criterion for distinguishing between an atomistically smooth and rough interface which is,

$$\eta_G = 1.5 \tag{4}$$

Just as g_m, the value of η_G as shown in equation (4) can also be used as a basis to distinguish between atomistically smooth interface and atomistically rough interface. Therefore, from equation (4), it is hypothesized that when $\eta_G > 1.5$, atomistically rough interface is expected, which should lead to a macroscopically non-faceted cellular morphology. And when $\eta_G < 1.5$, an atomistically smooth interface is expected, which should lead to a macroscopically faceted cellular morphology. In spite of the simplicity of equations (1) and (2), the analysis of the Cahn diffuseness theory has faced a major challenge because η_G is numerically inaccessible, since there is no direct way of knowing the value of ζ experimentally or computationally by any other known model, except by the current solidification model by the maximum entropy production rate (MEPR) principle [1], which forms the basis for further discussion in this paper.

On an exposition of thermal diffuseness

Analogous to the Cahn theory is the well-known Jackson criterion [12] which gives a qualitative insight into the roughness of an interface on macroscopic scale. For practical interpretation at the macroscopic scale, the Jackson criterion predicts the formation of a faceted and non-faceted morphology for pure materials by the equation [12]

$$\alpha_J = \frac{\Delta h_{sl}}{R_g T_m} \tag{5a}$$

where α_J (dimensionless) is commonly called the Jackson roughness factor or roughness criterion, Δh_{sl} ($Jmol^{-1}$) is the equilibrium heat of fusion, T_m (K) is the melting temperature of the material and R_g ($Jmol^{-1}K^{-1}$) is the universal gas constant. This model suggests that, when the α_J (dimensionless) is>2 then an atomistically smooth interface is predicted i.e., smooth macroscopic features (faceted morphology) are expected. And when the roughness criterion, α_J, is<2 then an atomistically rough interface (non-faceted morphology) is expected. The Jackson's criterion may imply that, materials with $2 \leq \alpha_J \leq 3$ may display as either faceted or non-faceted depending on the crystallographic orientation. Despite the considerable success achieved by the model, its main drawback has been that it does not consider the effect of temperature gradient, G_L (Km^{-1}) (or cooling rate) and the solidification velocity, V (ms^{-1}).

In this paper, the term thermal roughening is re-introduced, which is labelled η_α, and now called the Jackson thermal diffuseness, which is the inverse of the Jackson roughness factor given as,

$$\eta_\alpha = \frac{1}{\alpha_J} \tag{6a}$$

Equation (6a) was first suggested by Jackson but has never been utilized for any practical applications. Similar to equation (5a) the expected baseline criterion becomes,

$$\eta_\alpha = 0.5 \tag{6b}$$

Both theories of Cahn and Jackson are applicable to the morphological transformation of a plane front interface to cellular morphology for directional solidification of the Bridgman type. However, the issue with these two theories have been that they have been applied to interface growth independently without any established connection between them despite the expected correlation associated with them.

Role of entropy generation on the nature of the SLI

The SLI generated during directional solidification at a fixed velocity V (ms^{-1}) and imposed temperature gradient G_L ($K\,m^{-1}$) in the liquid can create an irreversible entropy due to the associated kinetic energy of the moving interface [1]. Also, the SLI which is a mixture a fully liquid melt and fully solid crystals generate configurational entropy as well as other entropy due to atom transfer from the liquid melt to the fully solid state. These entropy generation processes lead up to overall irreversible entropy generated which builds up within the SLI [6]. The SLI can stretch to accommodate entropy generated but is dependent on the nature of alloy (and solute concentration), the temperature gradient and the solidification velocity. When the entropy generated reaches a maximum, it is dissipated in a form that is used by the system to create diverse morphological features such as cellular morphology from the initial plane front. That is, the dissipated entropy considered in the form of heat energy can be captured as work lost by the SLI which is equivalent to the work done by the SLI to create the cellular shapes [1,8]. This mechanism is adopted by the SLI as a way of dissipating the free energy leading to the interface instability for the evolution of both faceted cellular and non-faceted cellular morphology from a plane front.

The objective of this paper is in three folds; the first is to evaluate the thickness of the solid–liquid interface at a fixed solidification velocity and temperature gradient to enable the computation of the diffuseness at the SLI. The second is to develop a mathematical relation to unify the concepts of the Cahn theory of interface diffuseness and the Jackson roughness criterion under the term, total diffuseness, η_T (dimensionless) based on a model by the maximum entropy production rate (MEPR) principle. The third is to use the total diffuseness to predict the formation of faceted cellular and non-faceted cellular morphology from a planar morphology i.e., evaluate the nature of the morphology that emanates from the interface at instability as a function of the solidification velocity and temperature gradient. The predictions would be compared with published experimental solidification data. The stated objectives would be achieved by employing a solidification model based on the maximum entropy production rate (MEPR) principle [1], which forms the basis for discussion in this paper. Note that, the maximum entropy production rate (MEPR), or the maximum entropy production principle (MEPP) are the acronyms mostly used in the literature for analyses that employ the entropy rate maximization principle [13,14,15,16,1,8,6]. However, the acronym MEPR [1,8] is used in this article to emphasize the importance of the term *rate* in the acronym.

Origin and derivation of entropy generation and maximization

During solidification of a liquid melt, the heat of fusion of the solid with defects, Δh_m ($J\ mol^{-1}$) and the equilibrium heat of fusion Δh_{sl} ($Jmol^{-1}$) within the SLI are related by [6],

$$\Delta h_{sl} = \Delta h_m + \omega_D \tag{7a}$$

where ω_D ($J\ m^{-3}$) is the energy of defects (such as grain boundaries or dislocations) per unit volume. In this work it is assumed that ω_D is a relatively small term and therefore equation (7a) becomes,

$$\Delta h_{sl} = \Delta h_m \tag{7b}$$

An entropy rate balance across the SLI which is the control volume is given by [1,6],

$$\frac{dS_{cv}}{dt} = \dot{S}_{in} - \dot{S}_{out} + \dot{S}_{gen} \tag{8}$$

where $\frac{dS_{cv}}{dt}$ ($J\ K^{-1}s^{-1}$) is the total steady state entropy rate change in the control volume, $\dot{S}_{in}$ ($J\ K^{-1}s^{-1}$) and $\dot{S}_{out}$ ($J\ K^{-1}s^{-1}$) are the rates of entropy entering and leaving the control volume respectively, and $\dot{S}_{gen}$ ($J\ K^{-1}s^{-1}$) is the irreversible entropy generation rate in the SLI. The rates of entropy entering ($\dot{S}_{in}$) and leaving ($\dot{S}_{out}$) the control volume is given by,

$$\dot{S}_{in} = A_{SLI}\, V\left(\frac{\Delta h_{sl}\,\rho_s}{T_{li}\,A_w} + s_{LG} + s_{SG}\right) \tag{9}$$

$$\dot{S}_{out} = A_{SLI}\, V\left(\frac{\Delta h_m\,\rho_s}{T_{si}\,A_w} + s_{SG}\right) \tag{10}$$

where the subscripts ($_{LG}$) and ($_{SG}$) refer to solute gradients in the

liquid and solid respectively, A_w (kgmol^{-1}) is the atomic weight of the solid, ρs (Kgm^{-3}) is the density of the solid, V (m s^{-1}) is the solidification velocity, S_{LG} (J m^{-3}K^{-1}) is the entropy generation density due to solute gradient in the liquid, SSG (J m^{-3}K^{-1}) is the entropy generation density due to solute gradient in the solid, A_{SLI} (m^2) is the area of the SLI and, T_{li} (K) and T_{si} (K) are liquidus and solidus temperatures at the boundaries of the SLI respectively. It is assumed that the thermal gradient across the SLI is linear and expressed as,

$$\Delta T_{SLI} = T_{li} - T_{si} = \zeta G_{SLI} \tag{11}$$

where G_{SLI} (K m^{-1}) is the linear temperature gradient across the SLI, and ΔT_{SLI} (K) is the temperature difference across the SLI. The volume of the solid–liquid interface Ω_{SLI} (m^3) is given as,

$$\Omega_{SLI} = A_{SLI}\ \zeta \tag{12}$$

A combination of equations (9) and (10) into equation (8) yields an expression of the control volume at steady state condition which is,

$$\frac{dS_{cv}}{dt} = \left(\frac{A_{SLI}\, V \Delta h_{sl}\, \rho_s}{T_{li} A_w} + A_{SLI} V\, s_{LG} + A_{SLI} V s_{SG}\right) - \left(\frac{A_{SLI}\, V \Delta h_m\, \rho_s}{T_{si} A_w} + A_{SLI} V\, s_{SG}\right) + \dot{S}_{gen} \tag{13a}$$

Further rearranging equation (13a) gives,

$$\frac{dS_{cv}}{dt} = \frac{A_{SLI}\, V \Delta h_{sl\,\rho_s}}{T_{li} A_w} - \frac{A_{SLI}\, V \Delta h_m \rho_s}{T_{si} A_w} + \Omega_{SLI}\, \dot{s}_{LG} + \dot{S}_{gen} \tag{13b}$$

Now dividing equation (13b) by the volume of the solid–liquid interface as expressed in equation (12), gives,

$$\frac{d\dot{s}_{cv}}{dt} = \frac{V \Delta h_{sl} \rho_s}{\zeta T_{li} A_w} - \frac{V \Delta h_m \rho_s}{\zeta T_{si} A_w} + \dot{s}_{LG} + \dot{s}_{gen} \tag{14}$$

where $\dot{s}_{gen}$ (J m^{-3}K^{-1}s^{-1}) is the total entropy generation rate density at the SLI, $\dot{s}_{LG}$ (J m^{-3}K^{-1}s^{-1}) is the entropy generation rate density by the solute gradient in the liquid and $\frac{d\dot{s}_{cv}}{dt}$ (J m^{-3}K^{-1}s^{-1}) becomes the total steady state entropy rate density in the control volume. From the assumption made from equation (7a) that $\Delta h_{sl} = \Delta h_m$, and applying the steady state condition, $\frac{d\dot{s}_{cv}}{dt} = 0$, to equation (14), then the total entropy generation rate density at the SLI becomes,

$$\dot{s}_{gen} = \left(\frac{V \Delta h_m \rho_s}{\zeta T_{si} A_w} - \frac{V \Delta h_m \rho_s}{\zeta T_{li} A_w}\right) - \dot{s}_{LG}$$

$$\dot{s}_{gen} = \frac{V \Delta h_m \rho_s (T_{li} - T_{si})}{\zeta A_w T_{li} T_{si}} - \dot{s}_{LG} \tag{15a}$$

Putting equation (11) into equation (15a) gives,

$$\dot{s}_{gen} = \frac{V \Delta h_m \rho_s G_{SLI}}{A_w T_{li} T_{si}} - \dot{s}_{LG} \tag{15b}$$

Both T_{li} and T_{si} are not readily known but for dilute binary alloy considerations, it can be approximated to be equal to T_m (K). Furthermore, the parameter G_{SLI} (Km^{-1}) which is the temperature gradient across the SLI which can be approximated as the average between the fully solid zone G_S (Km^{-1}) and the fully liquid zone G_L (Km^{-1}). However, due to the lack of obtaining reliable experimental data on the temperature gradient for the SLI and also for simplicity of computation, G_{SLI} is assumed to be approximately equal to the temperature gradient in the fully liquid zone, G_L (Km^{-1}), and i.e., $G_{SLI} \approx G_L$. Therefore equation (15b) becomes,

$$\dot{s}_{gen} = \frac{V \Delta h_m \rho_s G_L}{A_w T_m^2} - \dot{s}_{LG} \tag{16}$$

The entropy generated in the SLI is expected to be dissipated into the surrounding as the SLI moves during solidification. However, the entropy generated within the SLI can only be dissipated when the build-up reaches a maximum ($\dot{\varphi}_{max}$). This condition is essential for a morphological transition from a plane front into a cellular morphology. As such, equation (16) becomes,

$$\dot{\varphi}_{max} = \frac{V \Delta h_m \rho_s G_L}{A_w T_m^2} - \dot{s}_{LG} \tag{17a}$$

The subscript (max) is used to emphasize entropy production maximization for the plane front to cellular transition. Equation (17a) is written in simplified form as,

$$\dot{\varphi}_{max} = \dot{s}_E - \dot{s}_{LG} \tag{17b}$$

where $\dot{s}_E$ (Jm^{-3}K^{-1}s^{-1}) is the entropy production rate density due to exchange of matter at the SLI and $\dot{s}_{LG}$ (Jm^{-3}K^{-1}s^{-1}) which is the entropy production rate density due to solute gradient in the molten alloy which is given as, $\Delta T_O V^2 R_g \ln(1/k)/4 D_L m_L$ [1]. The term m_L (Km^{3}mol^{-1}) is the slope of the liquidus line of a binary phase diagram, k (dimensionless) is the partition coefficient that can be obtained from the binary phase diagram, D_L (m^{2}s^{-1}) is the coefficient of solute diffusion in the solvent of the alloy. The ΔT_O (K) is the solidification temperature range which is expressed as (T_l-T_s) or (C_o(1-k) m_L/k), where T_l (K) and T_s (K) are the liquidus and solidus temperatures respectively as can be obtained from the phase diagram, and C_o (molm^{-3}) is the solute concentration in the binary alloy. For dilute binary alloy considerations, both T_l and T_s can be approximated to be equal to T_m (K). Also, the maximum entropy production rate density $\dot{\varphi}_{max}$ (Jm^{-3}K^{-1}s^{-1}) has been given as [1],

$$\dot{\varphi}_{max} = \frac{\Delta \rho_k\, V^3}{2\, \zeta^2\, G_L} \tag{18}$$

The $\dot{\varphi}_{max}$ parameter quantifies the accumulated irreversible entropy generated at the SLI and the corresponding accumulation until it reaches a maximum. The dissipated entropy is responsible for the trigger of morphological instability and transition from one form to the other. Under the MEPR model approach, the established criterion for the morphological instability at the SLI for a binary alloy is given as [1]:

$$\left(\frac{\partial \dot{\varphi}_{max}}{\partial V}\right)_{\zeta,\ C_o} = 0 \tag{19}$$

For a mathematical evaluation of the morphological instability, the application of equation (19) to equation (18) and (17) gives [1],

$$\left(\frac{V}{G_L}\right)_C = \frac{D_L}{\Delta T_O} \frac{2\, m_L\, \Delta h_m\, \rho_s}{T_m^2\, A_w\, R_g \ln(1/k)} \tag{20}$$

where the subscript (c) refers to a morphological instability. Note that in some literature sources it is referred to as breakdown and denoted by the symbol (b).

Model

Solid-liquid diffuseness model

The size of the SLI can be evaluated at a solidification growth velocity by combining equations (17) and (18) to give,

$$\zeta = \frac{V\, T_m \sqrt{A_w}}{G_L \sqrt{\Delta h_m}} \sqrt{\frac{\Delta \rho_k}{\rho_s}} \sqrt{2 - \frac{V\, \Delta T_o\, R_g \ln(1/k)\, T^2_{m\, A_w}}{2\, G_L\, D_L\, m_L\, \Delta h_m\, \rho_s}}^{-1} \tag{21a}$$

The equation (21a) can be normalized with the interplanar spacing (d) as expressed in equation (2) to give the Cahn driving force diffuseness which represents the number of atomic layers within an interface for a binary alloy. This then gives,

$$\eta_G = \frac{V\, T_m \sqrt{A_w}}{G_L\, d \sqrt{\Delta h_m}} \sqrt{\frac{\Delta \rho_k}{\rho_s}} \sqrt{2 - \frac{V\, \Delta T_o\, R_g \ln(1/k)\, T^2_{m\, A_w}}{2\, G_L\, D_L\, m_L\, \Delta h_m\, \rho_s}}^{-1} \tag{21b}$$

For simplicity equation (21b) is written in condensed and compact form, which enables a dimensionless representation of the form,

$$\eta_G = M_d\sqrt{\Delta\rho_k/\rho_s}\ \sqrt{2-B_d}^{-1} \tag{21c}$$

where the expression $\left(V\,T_m\sqrt{A_w}/G_L d\sqrt{\Delta h_m}\right)$ is represented by the symbol M_d (dimensionless). The role of the component $\sqrt{A_w}T_m/d\sqrt{\Delta h_m}$ (Ksm^{-2}) in M_d is to modify the dimension of the V/G_L ($m^2s^{-1}K^{-1}$) ratio and to enable normalization of M_d into a dimensionless form. Note that the value of M_d is highly dependent on the V/G_L ratio ($m^2K^{-1}s^{-1}$), especially V which is the main variable in any typical directional solidification process.

The expression $\left(V\,\Delta T_o\,R_g\ln(1/k)\,T_M^2\,A_w/2\,G_L\,\rho_s\,D_L\,m_L\,\Delta h_m\right)$ is represented by the symbol B_d (dimensionless), where also the entire expression (2)-B_d) is dimensionless. The physical meaning of B_d is that it determines the maximum value of the interface thickness for a given binary alloy and at any given solidification growth velocity. The dimensionless value, $\Delta\rho_k/\rho_s$ is a material constant for a binary alloy that rarely changes at dilute solute concentration. The representation of the Cahn driving force diffuseness in equation (21c) in dimensionless form offer the advantage of presenting the interface diffuseness in a log–log plot of η_G against M_d, where $\sqrt{\Delta\rho_k/\rho_s}\sqrt{2-B_d}^{-1}$ is expected to be equivalent to the slope.

A size limit of diffuse interface

As derived in equation (21c), at any solidification velocity before interface instability becomes apparent, the value of (2-B_d) is expected to be greater than zero but<2 and likewise. The parameter $\Delta\rho_k/\rho_s$ is practically always less than one for all binary alloys. That is, the interface thickness as given in equation (21c) would approach its maximum value of positive infinity when the value of $(\Delta\rho k/\rho_S)/(2\text{-}Bd)$ becomes extremely large as Bd approaches 2.

$$\lim_{B_h\to 2}\eta_G(V) = +\infty \tag{22a}$$

The implication of equation (22a) is that the value of η_G practically does not exit at this condition. In other words, the interface will consequently dissolve into the molten fully liquid zone. However, when B_d approaches 2 such that $(\Delta\rho_k/\rho_s)/(2\text{-}B_d)$ is equal to one then equation (21c) becomes,

$$\eta_G = M_d \tag{22b}$$

The significance of equation (22b) is that, at this condition the density of the solidifying liquid remains constant and the flow of the molten liquid along the temperature gradient is incompressible till it transforms into completely fully solid phase. Moreover, the solidification velocity would always be linear with the diffuseness as compared to equation (21c). It is the simplest relationship of η_G with M_d, and this occurs when the solidification growth velocity is equal to the expression,

$$V = \frac{2\,G_L\,D_L\,m_L\,\Delta h_m}{\Delta T_o\,R_g\ln(1/k)\,T_{m\,A_w}^2}\,(2\rho_s-\Delta\rho_k) \tag{23}$$

On the other hand, the interface fades away when B_d becomes equal to 2 as in equation (21c), where at this point, the interface becomes undefined. Its practical significance is that the interface has become non-existent, and that solidification progresses without the formation of an interface. This occurs when the solidification growth velocity equal to

$$V = \frac{4\,G_L\,D_L\,m_L\,\Delta h_m\,\rho_s}{\Delta T_o\,R_g\ln(1/k)\,T_{m\,A_w}^2} \tag{24}$$

Also, at extremely low solidification growth velocity, $2\gg B_d$ as according to equation (21c) and the size of the interface becomes,

$$\eta_G = M_d\sqrt{\frac{\Delta\rho_k}{2\,\rho_s}} \tag{25}$$

It is expected from equation (25) that at such low solidification velocity, η_G would be far less than one. And that is, the interface size would be extremely small and can be considered as a sharp interface. The implication is that the atoms in the fully liquid phase will hop across the interface to occupy the lattice positions of the fully crystalline phase.

Diffuseness behaviour at a morphological instability

From an entropy generation approach, the morphological instability from plane front to cellular morphology occurs when the condition given in equation (19) is fulfilled. This can also be analyzed from an interface diffuseness point of view where instability can be described as when B_d is equal to one. Therefore, from equation (21c), the number of atomic layers at the SLI at the morphological instability is given as,

$$\eta_{G_C} = M_{dc}\sqrt{\frac{\Delta\rho_k}{\rho_s}} \tag{26a}$$

The physical meaning of M_{dc} is that it contains the key variables of solidification (V/G_L) in non dimensionalized form at instability. Hence putting in the expression for the solidification velocity at instability in equation (10) into equation (26a) gives,

$$\eta_{G_C} = \frac{2\sqrt{\Delta h_m}\sqrt{\Delta\rho_k}m_{L\ D_L}}{\mathbf{d}\Delta T_o\,R_g\ln(1/k)\,T_m} \tag{26b}$$

The result obtained in equation (26a) can be similarly obtained when equation (20) is put in equation (21b). Recalling equation (4) where η_G is used as a criterion for distinguishing between atomistically smooth and rough behaviour, and applying the criterion to equation (26a) becomes,

$$M_{dC} = 1.5\sqrt{\frac{\rho_s}{\Delta\rho_k}} \tag{27a}$$

That is, when η_G is 1.5 B_d is 1, and $\sqrt{\rho_s/\Delta\rho_k}$ is a material constant for dilute binary alloy consideration. Putting equation (20) into equation (27a) gives:

$$\frac{k}{(1-k)\ln(1/k)} = \eta_\alpha\,\frac{1.5\,C_o\,d\sqrt{A_w\Delta h_m}}{2\,D_L\sqrt{\Delta\rho_k\,\rho_s}} \tag{27b}$$

The equation (27b) gives a baseline relationship between Cahn's diffuseness concept and the Jackson's criterion for thermal diffuseness. It can be seen that, k/(1-k)ln(1/k) changes only when C_o changes. However, for very dilute binary alloy systems (when C_o is very small), the slope of the liquidus line (m_L) remains constant, and k/(1-k)ln(1/k) also remains the same irrespective of the fluctuations of C_o. Equation (27b) would be useful for obtaining data on the partition coefficient for thermodynamic consideration without the need for a phase diagram.

Model limiting conditions and the evolution of faceted and non-faceted morphology

One predictive tool of the model is for the determination of the evolution of either a faceted cellular or non-faceted cellular morphology at instability from a plane front. This can be achieved through further analysis of the model at different limiting conditions shown here. At a recall of equation (21c), the number of atomic layers present at the SLI can be rewritten in modified form to give,

$$\eta_G\sqrt{2-B_d} = M_d\sqrt{\frac{\Delta\rho_k}{\rho_s}} \tag{28a}$$

Further rearrangement of equation (28a) leads to,

$$\frac{\eta_G}{\sqrt{2-B_d}}\sqrt{2-B_d}\cdot\sqrt{2-B_d} = M_d\sqrt{\frac{\Delta\rho_k}{\rho_s}}$$

$$\frac{\eta_G}{\sqrt{2-B_d}}\left(\sqrt{2-B_d}\right)^2 = M_d\sqrt{\frac{\Delta\rho_k}{\rho_s}}$$

$$\frac{\eta_G}{\sqrt{2-B_d}}(2-B_d) = M_d\sqrt{\frac{\Delta\rho_k}{\rho_s}}$$

$$\frac{2\eta_G}{\sqrt{2-B_d}} - \frac{\eta_G B_d}{\sqrt{2-B_d}} = M_d\sqrt{\frac{\Delta\rho_k}{\rho_s}}$$

$$\frac{2\eta_G}{\sqrt{2-B_d}} = M_d\sqrt{\frac{\Delta\rho_k}{\rho_s}} + \frac{\eta_G B_d}{\sqrt{2-B_d}} \quad (28b)$$

It can be seen from equation (28b) that, the first term on the right-hand side (RHS) is the expression for the morphological instability as given in equation (26a). This implies the condition for a morphological transition from a plane front to a cellular form, and equation (28b) becomes,

$$\frac{2\eta_G}{\sqrt{2-B_d}} = M_d\sqrt{\frac{\Delta\rho_k}{\rho_s}} + \frac{\eta_G B_d}{\sqrt{2-B_d}} \quad (28c)$$

The expression for B_d on the numerator of the second term on the RHS of equation (28c) can be rearranged and expressed as,

$$B_d = \left(\frac{V\,\Delta T_o \ln(1/k)\,T_m\,A_w}{2\,G_L\,D_L\,m_L\,\rho_s}\right)\frac{R_g T_m}{\Delta h_m} \quad (29)$$

where the expression $R_g T_m/\Delta h_m$ is the Jackson thermal diffuseness, η_α as deduced in equation (6). Combining equations (28c) and (29) gives,

$$\frac{2\eta_G}{\sqrt{2-B_d}} = M_d\sqrt{\frac{\Delta\rho_k}{\rho_s}} + \frac{\eta_G}{\sqrt{2-B_d}}\left(\frac{V\,\Delta T_o \ln(1/k)\,T_m\,A_w}{2\,G_L\,D_L\,m_L\,\rho_s}\right)\eta_\alpha \quad (30a)$$

The condition for instability leading to the formation of cellular morphology from a plane front as shown in equation (26a), occurs at when B_d is equal to one, and therefore its implication on equation (30a) gives,

$$2\eta_G = \eta_{G_C} + \left(\frac{V^2 T_m^2\,\Delta T_o \ln(1/k)\sqrt{\Delta\rho_k}\;A_w^{3/2}}{2\,G_L^2\,d\,D_L\sqrt{\Delta h_m}\;m_L\,\rho_s^{3/2}}\right)\eta_\alpha \quad (30b)$$

At the morphological transition the expression in the parenthesis at the RHS of equation (30b) is expected to be small and therefore assumed to approach unity $\left(V^2 T_m^2\,\Delta T_o \ln(1/k)\sqrt{\Delta\rho_k}\;A_w^{3/2}/2\,G_L^2\,d\,D_L\sqrt{\Delta h_m}\;m_L\,\rho_s^{3/2} = 1\right)$. Also, the term $2\eta_G$ on the left-hand side (LHS) of equation (30b) is now designated as η_T, where η_T is the summation of the contributions of η_G and η_α, as given in equations (4) and (6), respectively. The symbol η_T (dimensionless), which is herein named as the total diffuseness, since it unifies both the diffuseness concepts by Jackson and Cahn [12,2]. This unification is attributed to the contributions from the disordering by both thermal energy and other driving forces for interface migration and morphological evolution. Equation (30b) finally becomes,

$$\eta_T = \eta_{G_C} + \eta_\alpha \quad (31)$$

Now, putting the values of equations (4) and (6) into equation (31) gives the value for η_T as,

$$\eta_T = 1.5 + 0.5$$

$$\eta_T = 2 \quad (32)$$

Equation (32) can be used as the baseline criterion for predicting the morphology that will emanate from the interface as either cellular faceted or cellular non-faceted at a morphological instability. Therefore, it is proposed that, when $\eta_T > 2$ a cellular non-faceted morphology is expected to emanate from the interface at instability and when $\eta_T < 2$ a cellular-faceted morphology is expected. The criterion derived from equation (32) is tested in this paper with available experimental data for directional solidification of binary alloy systems.

Results and discussions

The principle of MEPR states that if there are sufficient degrees of freedom within a system, it will adopt a stable state at which the entropy generation rate is maximized in an open thermodynamic system. The entropy generated at the SLI is dissipated by controlling the size of the interface by the magnitude of the V/G_L ratio. The MEPR model shows that, the interface thickness of a binary alloy can be calculated from data from directional solidification process when the V/G_L ratio is known, as shown in equation (21). The interface thickness becomes zero when the V/G_L ratio is zero.

The model is tested with data sets from table-2 which mainly are comprised of ten different binary alloys selected from different literature sources representing sixty-three experimentally measured data points at varying dilute concentrations (C_o) of the alloying elements. The experimental data were drawn from metallic binary alloys at instability conditions from plane front to cellular morphology. The instability solidification velocity V_C (ms^{-1}) and the corresponding imposed steady state temperature gradient in the liquid melt G_L (Km^{-1}) are also tabulated in table-2. The partition coefficient and the slope of both the solidus and liquidus lines can be calculated from the binary phase diagram. The data in tables 1 and 2 is summary of physical constants used in the calculations.

The figure-1 (a-c) is a log–log representation of equation (21c) describing the exponential growth type of relationship between the Cahn driving force diffuseness (thickness of the interface or number of atomic layers) as a function of M_d, where M_d is a strongly dependent on V/G_L considering a fixed solute composition and partition coefficient for different dilute binary materials. However, as the interface thickness is subjected to high velocities (i.e., increasing values of M_d) the slope of the curve changes quickly when (2 - B_d) becomes less than two which terminates at the point when B_d approaches two, which is the limit of the interface diffuseness as shown by equation (24).

The influence of varying solute composition on the Cahn driving force diffuseness is highlighted in Fig. 1(d) with the compositions spanning four orders of magnitude in the dilute concentration range. Figure-1d further shows that the higher the solute concentration the quicker the system triggers an instability condition. This is because, the

Table 1
Some physical constant of the solvents of the binary alloys in pure form.

Element	Atomic weight ($Kgmol^{-1}$) [17]	Melting temperature T_m (K)	Density ρ_s of the solvent at room temperature (Kgm^{-3}) [18]	Density (ρ_l) of liquid at T_m (Kgm^{-3}) [18]	Heat of fusion Δh_m ($Jmol^{-1}$)
Al	0.027	933.6 [19]	2700	2385	10,470 [18]
Bi	0.209	554.6 [20]	9790	10,050	11,106 [21]
Pb	0.207	600.6 [22]	1134	10,678	4810 [18]
Sn	0.119	505.1 [23]	7260	6980	7080 [18]

Table 2
Experimentally measured solidification parameters for planar to cellular morphological change for dilute binary alloys.

Alloy	Solute conc C_o (wt %)	Temp gradient G_L (Km^{-1})	Critical velocity V_C (μms^{-1})	Diffusivity at infinite dilution D^O (m^2s^{-1})	Activation energy of diffusion Q_D ($Jmol^{-1}$)	Experimental temperature range for measurement (K)	Quantification Method
Al-Cr [24]	0.102	2080	61.9	2.18×10^{-5}	−88000	1008.2–1173.2	Rotating Disc [25]
	0.102	1610	39.6				
	0.201	2090	25				
	0.201	2300	26.6				
	0.328	2990	29.2				
	0.328	3040	28.2				
	0.328	3060	25.4				
	0.328	2810	26.3				
	0.328	2940	26.2				
	0.328	3050	23				
Al-Cu [26,27,28,29]	0.025	920	22	1.8×10^{-7}	−24700	963.2	Finite Column [30]
	0.025	1170	48				
	0.47	1450	17.5				
	0.20	2500	12				
	0.73	2000	22				
Al-Ti [24]	0.024	4280	18.8	1.49×10^{-7}	−33330.65	973.2	Rotating Disc [31]
	0.054	3870	5.35				
Al-Zn [32]	0.083	1120	47.4	2.99×10^{-5}	−68400	973.2	[33]
	0.083	840	33.6				
	0.083	970	36.7				
	0.096	2650	65.9				
	0.096	2310	64.5				
	0.096	2040	54.5				
	0.375	1310	8.55				
	0.375	1430	10.3				
	0.375	1570	12.1				

Alloy	Solute conc C_o (wt %)	Temp gradient G_L (Km^{-1})	Critical velocity V_c (μms^{-1})	Diffusivity at infinite dilution D^O (m^2s^{-1})	Activation energy of diffusion Q_D ($Jmol^{-1}$)	Experimental temperature range for measurement (K)	Quantification Method
Pb-Ag [34]	0.0001	470	167	2.13×10^{-8}	−6004.69	663.2–1058.2	Long capillary cell [35]
	0.00025	770	125				
	0.0005	1080	67				
	0.00075	1250	46				
Pb-Sn [34]	0.01	540	167	4.9×10^{-8}	−16915.91	523.2–873.2	Capillary-Reservoir [36]
	0.03	820	73.5				
	0.05	1380	73.5				
	0.06	1220	75				
	0.1	1200	56.7				
	0.15	1300	33.3				
	0.15	415	108				
	0.15	465	142				
	0.15	485	167				
	0.15	700	230				
Pb-Bi [37]	0.1	2500	14.3	2.76×10^{-8}	−13700	645.2–773.2	Capillary-Reservoir [38]
	0.2	2500	7.86				
	0.3	2550	5.1				
Pb-Sb [39]	0.0089	1020	27.54	2.01×10^{-8}	−9591.49	663.2–1058.2	Capillary Diffusion [35]
	0.0179	1030	13.77				
	0.0179	1035	11.95				
	0.0179	1045	11.31				
	0.0265	1055	8.23				
	0.0354	1060	7.36				
Sn-Pb [40]	0.0024	2100	110	4.4×10^{-8}	−12694.26	523.2–873.2	Capillary-Reservoir [36]
	0.006	2200	130				
	0.015	4400	44				
	0.02	2800	32				
	0.02	3400	32				
	0.02	4000	32				
	0.0015	1700	260				
	0.012	5000	63				
	0.0046	2300	170				
	0.012	3100	63				
	0.012	4200	63				
	0.012	4400	63				
Bi-Sn [41,42]	0.0568	21,630	13.3	5.52×10^{-8}	−13828.59	723–873	[43]

higher the solute concentration the greater the entropy is generated to necessitate the development of new morphology to form. From Fig. 2, the Cahn driving force diffuseness is approximately noted to be small and up to a maximum of 834 lattice spacings. The relationship between the Cahn driving force diffuseness and dimensionless parameter M_d is for a host of experimental data points which yields a straight line as per equation (26a) irrespective of material parameters for any growth direction (or any crystal plane spacing normal to a growth direction). All the binary alloys yield a atomistically rough interface at instability except Bi-Sn which shows atomistically smooth interface. These

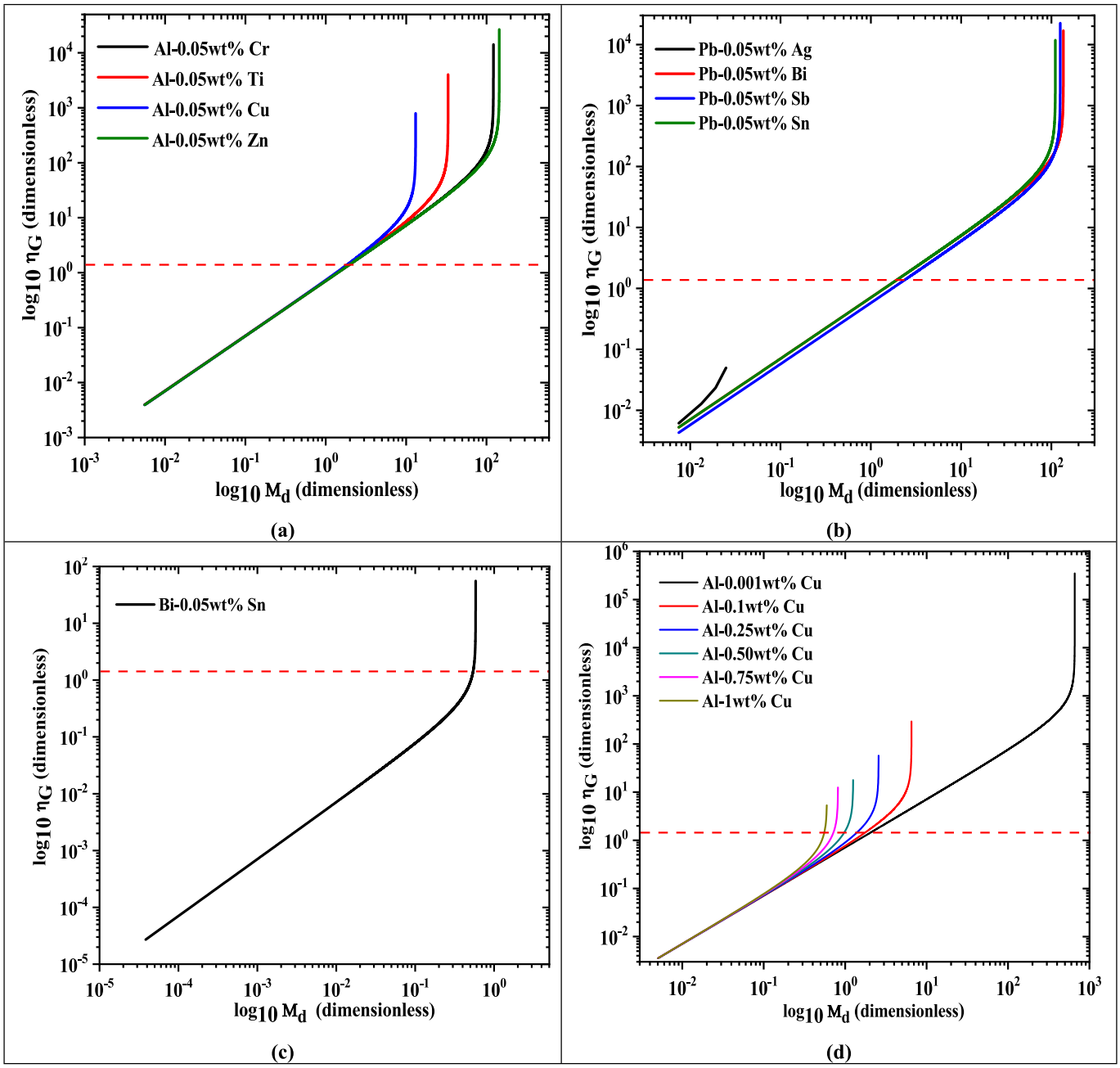

Fig. 1. (a-d): The model prediction showing the relationship between Cahn driving force diffuseness, η_G, and the dimensionless parameter, M_d for different dilute binary materials as given in equation (11c). The dotted horizontal red line indicates the criterion between atomistically smooth and atomistically rough interface as given in equation (4). Materials existing above the red dashed line have atomistically rough interface and materials below have atomistically smooth interface. There is no diffuseness at high V/G_L when ($2\text{-}B_d$) turns zero. The sudden increase in slope at high V/G_L ratio occurs when ($2\text{-}B_d$) becomes less than one. Fig. 1(d) shows for Al-Cu at different solute concentrations and displays linear forms at low velocities and changes slope at higher velocities. At extremely low concentration the relationship approaches linearity. (For interpretation of the references to colour in this figure legend, the reader is referred to the web version of this article.)

deductions from Fig. 2 are all in accordance with experimental observations. However, there is one Bi-Sn data point that show atomistically smooth interface but close to the transition line. The implication is that, at this data point the interface can transition to atomistically rough interface at an increased solidification growth velocity. The result given in Fig. 2 satisfies the predictions made in Fig. 1.

The horizontal dotted-red line in Figs. 1 and 2 corresponds to an approximately 1.5 atomic layer of the material formed at the interface as predicted according to equation (4). The binary alloys that solidify above the horizontal red-dotted line in Figs. 1 and 2 are expected to display atomistically rough interface features which should correspond to cellular non-faceted morphology. Solidification below the horizontal red-dotted line indicates atomistically smooth features which should correspond to cellular faceted morphology.

It should be noted that the faceted and non-faceted morphologies only emanate from a planar interface when the instability criterion given by equation (19) is fulfilled. In relation to the Cahn driving force diffuseness, the maximum entropy generation rate density increases with the corresponding decrease in diffuse interface thickness (diffuseness) which leads a morphological instability of a non-planar

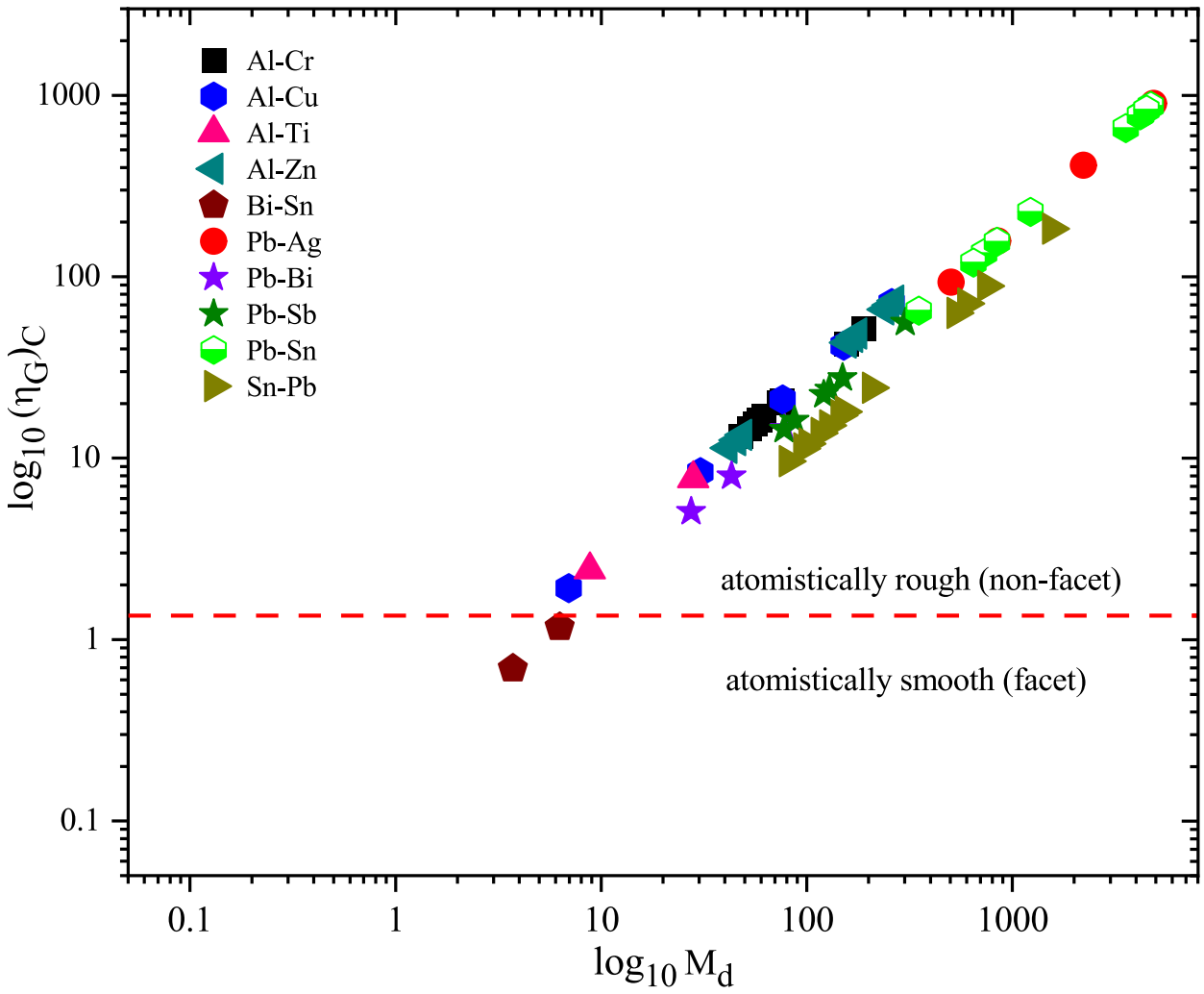

Fig. 2. The relationship between Cahn driving force diffuseness, $(\eta_G)_C$ and dimensionless parameter $(M_d)_C$ at the condition of morphological instability. The plot shows measured experimental solidification parameters at instability in the abscissa and calculated interface diffuseness on the ordinate. The horizontal dotted-red line indicates the criterion between atomistically smooth (corresponding to a faceted morphology) to atomistically rough (corresponding to a non-faceted morphology) regimes as given by equation (4). Materials above the dotted-red line are atomistically rough and materials below are atomistically smooth. The data for the plot are given in tables-1 and 2. (For interpretation of the references to colour in this figure legend, the reader is referred to the web version of this article.)

morphology when B_d approaches 1 as according to equation (26a).

From Fig. 3 shows the calculated total diffuseness plotted against the dimensionless parameter M_d where the $(V/G_L)_C$ values are experimental parameters at the morphological instability condition. All points in Fig. 3 are labelled as either faceted or non-faceted according to equation (32). The horizontal dotted-red line again serves as the transition line between the two regimes and represents a double atomic layer for the smallest interplanar spacing growing along a selected crystallographic plane as per the derivation in equations (31) and (32). The binary alloys that fall above the dotted-red horizontal line are materials that show non-faceted cellular morphology during morphological instability condition. And the alloys that fall below the dotted-red horizontal line show faceted cellular morphology during interface instability condition.

For several materials like the Al alloys and Pb-Sn alloys the diffuseness is large i.e., contains many atomic layers. The high interface diffuseness calculated for some of the alloys are perhaps not unusual. Experimental evidence of large interface thickness as thick as 1 μm in size has been reported in Al-Cu alloys [44]. In the phase field literature, the number of atomic layers in a diffuse interface region [45], can vary between 2 and 2750 lattice spacings though it is usually an a priori assumption made of the interface thickness. The binary alloys (Al-Cr, Al-Cu, Al-Ti, Al-Zn, Pb-Ag, Pb-Bi, Pb-Sb, Pb-Sn, and Sn-Pb) in Fig. 3 show non-faceted morphology while Bi-Sn displays faceted cellular morphology at interface instability which agrees with all experimental observations. Again, Fig. 3 further shows that a transition from faceted cellular to non-faceted cellular morphology is highly probable for certain alloys predicted by the MEPR model depending on the solidification conditions [11]. There is currently a paucity of experimental data regarding faceted cellular transformations for binary alloys apart from Al_2O_3-MgO [46] where the transition from faceted cellular to non-faceted cellular and again to a faceted cellular morphology was reported [11]. Similar results have also been noted earlier by Jackson and Miller [47] in undercooled alloys for hexachloroethane and ammonium chloride; by Glicksman and Schaeffer [48] for white phosphorus and by Shangguan for salol [49].

For practical considerations, this model can be used to analyze the stability and behavior of solid–liquid interfaces during solidification/crystal growth processes. It can also provide valuable insights into the growth behaviour and morphological features associated with crystal transformation and development for practical applications. Furthermore, the model can serve as an essential tool for providing fundamental insights and understanding that can support experimental observations

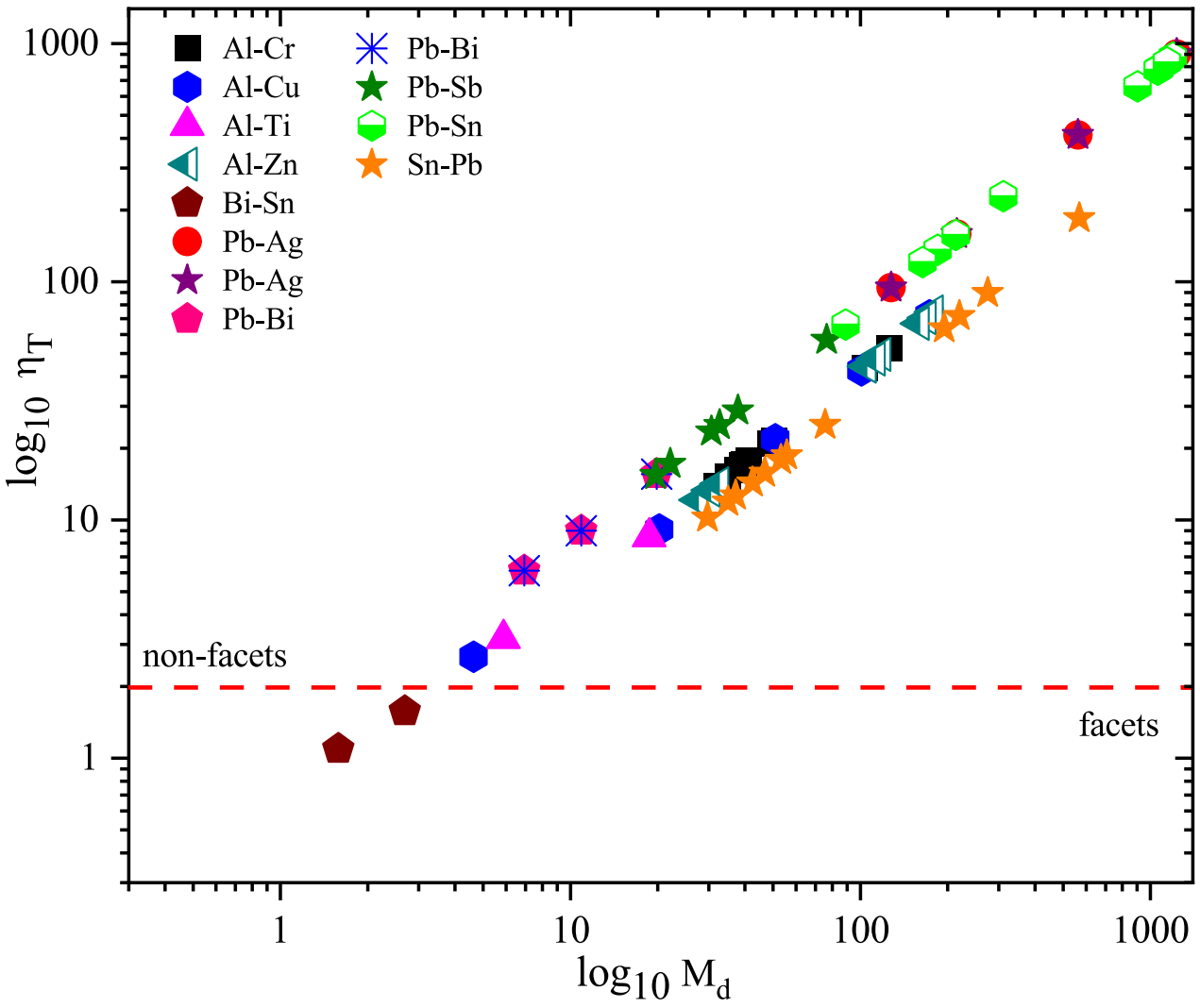

Fig. 3. The relationship between total diffuseness and dimensionless parameter M_d at instability conditions yields a straight line as per equation (26a) irrespective of material parameters for any growth direction (or crystal plane spacing normal to a growth direction). The plot above shows measured experimental conditions at instability in the abscissa and calculated total diffuseness on the ordinate. The total diffuseness is the sum of both $(\eta_\alpha + \eta_G)$. If the total diffuseness is greater than two then there is a possibility of non-faceted cellular morphology at instability, otherwise it should be faceted cellular morphology. The values V_C and G_L are experimentally measured numbers at instability and η_T is calculated from the model. Experimentally, the materials shown below the dashed line ($\eta_T = 2$) are recorded to be macroscopically faceted. The data for the plot are given in Tables 1 and 2.

and to help shape the development of crystal growth techniques for many industrial applications.

Summary and conclusion

An interface structure and diffuseness model has been presented to explain the transition from a plane front to cellular morphology for binary alloys. The model at the limiting conditions is able to mathematically unify Cahn diffuseness theory and the Jackson roughness criterion through the evaluation of the thickness of the solid–liquid interface at a fixed solidification velocity and temperature gradient to attain the total diffuseness. The key MEPR condition for interface diffuseness or topographical change is primarily related to the maximum entropy production rate density which is a function of the composition, solidification velocity, the temperature gradient, and the partition coefficient when a solute gradient in the liquid is established. The MEPR model hypothesizes that entropy generation is maximized when an interface transition occurs at a different configuration whether an atomistic or a topographical variant. This interface structure and diffuseness model tested for by varying amounts of aluminium, lead, and tin binary alloys, and can quantitatively predict the size of a diffuse interface and the number of atomic layers present. Analysis and test of the diffuseness model with experimental data shows that the model can account for the interface morphology as being either faceted cellular or non-faceted cellular morphology. The interface structure and diffuseness model also show a transition point from faceted to non-faceted cellular morphology when the number of atomic layers is above two.

Declaration of Competing Interest

The authors declare that they have no known competing financial interests or personal relationships that could have appeared to influence the work reported in this paper.

Data availability

All data are in the manuscript.

Acknowledgement

The encouragement by Maame Afia Pokuaa Bensah during this work is appreciated. Appreciation to Ms. Gwendolyn Naa Oyo Quartey for reading through the manuscript.

Authors' contributions

This work was solely done by the author.

Funding sources

There was no external funding to this work. The work was supported through personal funds.

Data availability statement

The data set used is given in tables-1 and 2.

Ethical statement

This research manuscript in my own original work which has not been published anywhere else.

References

[1] Bensah YD. Morphological linstability at the solid-liquid interface by the maximum entropy production rate principle. Can J Phys 2018;96(12):1314–20.
[2] Cahn JW. Theory of crystal growth and interface motion in crystalline materials. Acta Metall 1960;8(8):554–62.
[3] Cahn JW, Hillig WB, Sears GW. The molecular mechanism of solidification. Acta Metall 1964;12:1421–39.
[4] Hoyt JJ, Asta W, Karma A. Method for computing the anisotropy of the solid-liquid interfacial free energy. Phys Rev Lett 2001;86(24):5530–3.
[5] Bensah YD, Sekhar JA. Morphological Assessment With The Maximum Entropy Production Rate Postulate. Curr Opin Chem Eng 2014;3:91–8.
[6] Sekhar JA. The description of morphologically stable regimes for steady state solidification based on the maximum entropy production rate postulate. J Mater Sci 2011;46(19):6172–90.
[7] Bensah YD, Sekhar JA. Solidification Morphology and Bifurcation Predictions with the Maximum Entropy Production Rate Model. Entropy 2020;22(40):1–3.
[8] Bensah YD. Evolution of cellular morphology in pure materials. J Mater Sci 2020:1–16.
[9] Frank FC. Influence of dislocations on crystal growth. Discuss Faraday, Soc 1949;5:48–54.
[10] Burton WK, Cabrera NT, Frank FC. The growth of crystals and the equilibrium structure of their surfaces. Phil Trans A 1951;243:299.
[11] Bensah YD. Morphological growth criterion for faceted to non-faceted transition in pure materials. Results Phys 2023;48(106418):1–9.
[12] Jackson KA. In: Liquid metals and solidification. Cleveland: American Society for Metals; 1958.
[13] Wang H, Liu F, Zhai H, Wang K. Application of the maximal entropy production principle to rapid solidification: A sharp interface model. Acta Mater 2012;60:1444–54.
[14] Martyushev LM, Seleznev VD, Kuznetsova IE. Application of the Principle of Maximum Entropy production to the analysis of the morphological stability of a growing crystal. Zh Éksp Teor Fiz 2000;118:149.
[15] Ziegler H, Wehrli C. On a principle of maximal rate of entropy production. J Non-Equilib Therm 1978;12:229.
[16] Veveakis E, Regenauer-Lieb K. Review of extremum postulates. Curr Opin Chem Eng 2015;7:40–6.
[17] IUPAC. Atomic weight of elements. Handbook 1981;55(7):1101–36.
[18] W. F. Gal and T. C. Totemeier(editors), "Smithells metals reference book," *Elsevier Inc.*, vol. 8th edition, 2004.
[19] Murray JL. The Al-Cr (Aluminum-Chromium) System. J Phase Equilib 1998;19(4):368–75.
[20] Predel B, Schwerman W. Analysis of the Thermodynamic Properties of Solid Pb-Bi Alloys. Zeitschrift für Metallkunde 1967;58:553–7.
[21] L. V. Gurvich, I. V. Veyts and C. B. Alcock, Thermodynamic properties of individual substances, New York: Hemisphere Publishing Corp., 1991, 4th edition, vol.2.
[22] Karakaya I, Thompson WT. The Ag-Pb (Silver. Lead) System. Bull Alloy Phase Diagr 1987;8(4):326–34.
[23] Karakaya I, Thompson WT. The Pb– Sn (Lead-Tin) system. Bull Alloy Phase Diagr 1988;9(2):237–43.
[24] Shibata K, Sato T, Ohiro G. Morphological stabilities of planar solid-liquid interfaces during unidirectional solidification of dilute Al-Ti and Al-Cr alloys. J Cryst Growth 1978;44(4):419–34.
[25] N. Tunca, G. W. Delamore and R. W. Smith, "Corrosion of Mo, Nb, Cr, and Y in Molten Aluminum," *Metallurgical transactions A,* vol. 21A, p. 2919=2928, 1990.
[26] Sato T, Ohira G. The cellular breakdown of the planar interface in unidirectional solidification of Al-Cu alloy. J Jpn Inst Metals 1970;34:690.
[27] Radojevic V, Nikolic S, Valcic A. Interface shape and distribution of solute during vertical Bridgeman growth of Al-Cu alloy. Mater Lett 2002;52:248–54.
[28] Fornaro O, A.Palacio H, Biloni H. Segregation substructures in dilute Al–Cu alloys directionally solidified. Mater Sci Eng A 2006;417(1-2):134–42.
[29] Grange G, Jourdan C, Gastaldi J. In situ observation of synchrotron white beam X-ray topography of the solidification microstructures of an Al-0.73wt% Cu alloy. J Cryst Growth 1992;121:315–21.
[30] Nathan Lee L, Cahoon J. Interdiffusion of Copper and Iron in Liquid Aluminum. J Phase Equilibria Diffus 2011;32(3):226–34.
[31] Lee JR. Liquidus-solidus in the system iron-aluminum. J Iron Steel Inst 1960;2:222–4.
[32] Sato T, Itp K, Ohira G. Interfacial stability of planar solid-liquid interface during inidirectional solidification of Al-Zn alloy. Trans Jpn Inst Metals 1980;21(7):441–8.
[33] Kim HS, Stone IC, Cantor B. Microstructural evolution in semi-solid AA7034. J Mater Sci 2008;43:1292–304.
[34] Tiller WA, Rutter JW. The effect of growth conditions upon the solidification of a binary alloy. Can J Phys 1956;34(1):96–121.
[35] Smith RW, Yang BJ, Huang WD. The measurement of solute diffusion coefficients in dilute liquid alloys: The influence of unit gravity and G-jitter on bouyancy convection. Ann NY Acad Sci 2004;1027:110–28.
[36] Davis KG. Diffusion Constants in Liquid Lead-Tin Alloys. Can Metall Q 1966;5(3):245–63.
[37] Billia B, Jamgotchian H, Capella L. Unidirectional solidification of dilute Pb-Bi alloys. Acta Metall 1981;29:1785–9.
[38] Masataka T, Toyota Y, Harada M, Eguch W. Mutual diffusion coefficient in molten lead-bismuth mixtures. J Chem Eng Japan 1983;16(2):92–8.
[39] Morris IR, Winegard WC. The development of cells during solidification of a dilute Pb-Sb alloy. J Cryst Growth 1969;5:361–75.
[40] Walton D, Tiller WA, Rutter JW, Winegard WC. Instability of a Smooth Solid-Liquid Interface During Solidification. J Metals, AIME Trans 1955;205:1023–6.
[41] Stenzel H, de Groh III H, Leonardi E, Timchenko V, de Vahl Davis G. Directional solidification of Bi-Sn on USMP-4. Mater Sci Forum 2000;329-330:235–46.
[42] R. Abbaschian, A. B. Gokhale, J. J. Favier, G. Cambon, S. R. Coriell, H. C. de Groh III and R. L. DeWitt, "A study of directional solidification of faceted Bi-Sn in microgravity," in *33rd Aerospace sciences meeting and exhibit*, Reno-Nevada, 1995.
[43] Pasternak AD, Olander DR. Diffusion in liquid metals. AIChE J 1967;13(6):1052–7.
[44] McKeown JT, Kulovits AK, Liu C, Zweiacker K, Reed BW, LaGrange T, et al. In situ transmission electron microscopy of crystal growth-mode transitions during rapid solidification of a hypoeutectic Al–Cu alloy. Acta Mate 2014;65:56–68.
[45] Gurevich S, Karma A, Plapp M, Trivedi R. Phase-field study of three-dimensional steady-state growth shapes in directional solidification. Phys Rev E 2010;81:1–15.
[46] Sekhar JA, Bharti A, Trivedi R. Faceted-nonfaceted dendritic transitions during the laser Processing of Al203-1.0 Wt Pct MgO. Metall Trans A 1989;20A:2191–4.
[47] Jackson KA, Miller CE. Experimental observation of the surface roughening transition in vapour phase growth. J Cryst Growth 1977;40:169–72.
[48] Glicksman ME, Schaeffer RJ. Investigation of solid-liquid interface temperatures through isenthalpic solidification. J Cryst Growth 1967;1:297–310.
[49] D. Shangguan, "PhD Thesis," University of Oxford, Oxford, 1989.